Prediction of stitch crack evolution and gas permeability in multidirectional composite laminates

Jianlong Xu, Bhavani V. Sankar

PII: S1359-835X(08)00188-7
DOI: 10.1016/j.compositesa.2008.07.003
Reference: JCOMA 2261

To appear in: *Composites: Part A*

Received Date: 27 October 2007
Revised Date: 10 July 2008
Accepted Date: 14 July 2008

Please cite this article as: Xu, J., Sankar, B.V., Prediction of stitch crack evolution and gas permeability in multidirectional composite laminates, *Composites: Part A* (2008), doi: 10.1016/j.compositesa.2008.07.003

PREDICTION OF STITCH CRACK EVOLUTION AND GAS PERMEABILITY IN MULTIDIRECTIONAL COMPOSITE LAMINATES

Jianlong Xu[1] and Bhavani V. Sankar[2]

Department of Mechanical and Aerospace Engineering, University of Florida
P.O. Box 116250, Gainesville, Florida, 32611-6250, USA

ABSTRACT

Stitch cracks in multidirectional laminates were observed by many researchers in the literature. In the current work, the damage evolution in multidirectional laminates is investigated using the strain energy release rate concept. Two methods are used to compute the strain energy release rate. The effects of ply angle and ply thickness on stitch crack evolution are investigated. Then, a model based on Darcy's Law for porous materials is developed for predicting gas permeability in composite laminates containing micro-cracks and delaminations. Gas permeability is presented as a function of crack density and crack intersection area. Then the intersection areas formed by crack opening displacements are computed using 3-D finite element analysis. The progressive gas permeability in multidirectional laminates is predicted and compared with the gas permeability predicted in the cross ply laminates in our previous work.

Keywords: A. Laminates; A. Polymer-matrix composites (PMCs); C. Finite element analysis (FEA); Permeability

INTRODUCTION

Weight reduction is one of the main goals in the development of cryogenic propellant tanks for future space vehicles. Lightweight fiber reinforced composite

[1]Graduate Student, xujl@ufl.edu.
[2] Newton C. Ebaugh Professor, Corresponding Author, Phone: (352) 392-6749, Fax: (352) 392-7303, Email: Sankar@ufl.edu .

materials are the major candidates for various gas tanks in space vehicles. Gas leakage found in X-33 hydrogen tank, however, has caused a setback to further application of composite materials in cryogenic tanks. Hence, understanding the mechanism of gas leakage through composite laminates is critical to the future application of composite materials in cryogenic storage tanks.

Recently, many experimental [1-9] and analytical [7-8, 10-14] works have been done to investigate gas permeability in composite laminates. Most of the analytical works have focused on cross-ply laminates, in which complete transverse matrix cracks developed to form the gas leakage path. Aoki et al. [7] conducted experiments on $[0_2/90_2]_s$ laminates and verified the gas leakage path formation using three-dimensional finite element method. Kumazawa et al. [8] performed leak analysis in laminates with stacking sequence of $[0/0/90/90]_s$ and compared with experimental results. Roy and Benjamin [10] developed permeation model based on Darcy's law and computed crack opening displacement based on the first-order shear deformable laminate theory. They applied their analysis to a $[0/90_2]_s$ cross-ply graphite/epoxy laminate. Xu and Sankar [11] parametrically investigated gas permeability in cross-ply laminates using three-dimensional finite elements.

Generally, it is good to include angle plies in composite design to gain better performance. It has been observed that the pattern of cracks in multidirectional laminates is quite different from that in cross-ply laminates [5, 16-19]. In cross-ply laminates, extensive transverse matrix cracks are observed. In multidirectional laminates, however, short cracks (also called stitch cracks) appear in angle plies depending on the ply angle and the ply thickness. Some researchers considered stitch cracks in their permeation models. Noh et al. [12] and Peddiraju et al. [13-14] set up a

damage network through laminates with the assumed stitch crack length and delamination, and then predicted the gas leakage rate using a computational fluid dynamics program (FLUENT©). Roy and Nair [15] developed a simple model to incorporate the stitch crack into their framework based on the first-order shear deformable theory by introducing an effective spring stiffness. In the above models, damage state was assumed, i.e., stitch crack lengths and stitch crack densities were assumed.

In the present work, an investigation using the concept of strain energy release rate is performed on the laminates with stacking sequence $[0/\theta_n/90]_s$. Some experimentally observed phenomenon are explained and predicted. The formation of the stitch crack (stitch crack length and stitch crack density) is predicted. And then a special scenario is taken to simulate the gas leakage through the laminates based on Darcy's law. The predicted gas permeability is compared with the permeability predicted in cross-ply laminates. The finite element analysis (FEA) was performed using the commercial package ABAQUS 6.5™.

PREDICTION OF STITCH CRACK EVOLUTION

Stitch cracks were first identified by Jamison et al. [20] under fatigue loading and then were systematically investigated by Lavoie and Adolfsson [16] in laminates with stacking sequence $[+\theta_n/-\theta_n/90_{2n}]_s$. It was found that stitch cracks not only emanated under fatigue loading but also emanated under monotonic loading and due to thermal residual stresses. Bechel et al. [5] also observed stitch cracks in $[0/+45/-45/90]_s$ laminates after certain numbers of thermal cycling. Yokozeki et al. [17-19] performed experiments on laminates of type $[0/\theta_n/90]_s$ and they found that whether stitch cracks or developed cracks will emanate in the θ^o-ply depended on the value of θ and the

thickness of the θ^o-ply. For large angle θ and thick angle ply, long cracks developed in the θ^o-ply, and for small angle θ and thin angle ply, stitch cracks developed in the θ^o-ply.

In the present work, the same laminate configuration $[0/\theta_n/90]_s$ as in Refs. [17-19] is considered. The ply thickness is taken to be 0.14 mm. The orthotropic material properties are listed in Table I, where E, G, v and α, respectively, are Young's moduli, shear moduli, Poisson's Ratio and coefficient of thermal expansion. As shown in Fig. 1A, the vertical lines represent the transverse matrix cracks developed in the 90^o-ply and the short-oblique lines represent the stitch cracks developed in the θ^o-ply. In the current model, it is assumed that both the transverse cracks in the 90^o-ply and the stitch cracks in the θ^o-ply are evenly distributed and all the stitch cracks have the same crack length. Hence, a unit cell containing one stitch crack can be taken as shown in Fig. 1B. It can be seen that for a specific specimen the unit cell can be described using three parameters: the spacing of transverse crack l_x, the spacing of stitch crack l_y, and the stitch crack length $2a$. Due to symmetric lay-up, only one-half of the unit-cell is analyzed as shown in Fig. 1C.

The dependence of strain energy release rate (SERR) on the three parameters (a, l_x, l_y) is investigated. Two methods are used to compute the SERR: the definition of SERR and the J-integral at the crack front. In the first method, the total strain energy in the unit cell is computed before and after stitch crack propagation, and then the SERR is obtained by taking the difference in the strain energy divided by the new generated crack surface area during propagation. In the second method, three-dimensional J-integrals along the stitch crack front are computed using the commercial finite element program ABAQUS. In the 3-D model, the crack tip is a

line and the 3D contour is normal to the crack front, and the program calculates the total energy release rate. The distribution of the J-integrals along the crack tip is not uniform. Hence, the average of the J-integrals is taken as the SERR. Figure 2 shows the comparison of the two methods with the same unit cell. It can be seen that the SERR computed from the two methods agree with each other quite well and converge to the same value as the crack length increases. In the following investigation, the J-integral method will be used in most cases and the other method will be used when the J-integral method is not applicable.

First, spacing l_x and l_y are fixed and the variation of the SERR with respect to the stitch crack length a is investigated as presented in Fig. 3. Two lay-ups considered here are: $[0/60/90]_s$ and $[0/30/90]_s$. In the present model, periodic boundary conditions are applied to obtain unidirectional loading state: $\varepsilon_x = \varepsilon_0$ and $\varepsilon_y = 0$. First, only mechanical loads are applied. The SERR computed from J-integrals are plotted in the solid line with square symbols. It can be seen that for strain levels $\varepsilon_x = 1\%$ and $\varepsilon_y = 0$ the value of SERR is around 100 J/m^2, which is much lower than the microcracking fracture toughness G_{mc} available in the literature [21]. It means that no crack will form at this strain level, which is not true from experimental observations. Hence, the effect of thermal residual stresses has to be included. The SERR due to thermal residual stress is computed when the unit cell is under the zero strains ($\varepsilon_x = \varepsilon_y = 0$) and the temperature decreases from the curing temperature (177^{o}C) to the room temperature (27^{o}C). Then the computed SERR due to thermal residual stresses is included in the total SERR using the approximate equation shown below [22]:

$$G^{Total} = G_M + G_T + 2\sqrt{G_M G_T}\sin\theta \qquad (1)$$

where G_M and G_T are the SERRs under mechanical loading and under thermal loading, respectively, and θ is the fiber direction in the angle ply .

It has been found that G_T itself is very low (around 10 - 20 J/m^2) but it has a great effect on the total SERR. From Fig. 3, it can be seen that after including thermal effect the total SERR increases to around 250 J/m^2, which is comparable to the microcracking fracture toughness G_{mc}. Hence, it is necessary to take the thermal stress effects into account. In this study we assume temperature independent properties for the ease of calculations. Procedures including temperature dependent properties were discussed by the authors in [11].

From experimental observations [17-19], for the same thickness of θ^o-ply, the stitch crack is more likely to develop in the $[0/\theta/90]_s$ laminates with a bigger value of θ. It can be easily seen from Fig. 3 that the SERR in the $[0/60/90]_s$ laminate drops down significantly after it reaches the maximum, while the SERR in the $[0/30/90]_s$ laminate drops down a small amount from the peak and then reaches a plateau. Hence, if the SERR in the $[0/60/90]_s$ laminate decreased below the microcracking fracture toughness, then the stitch crack would stop propagating. Meanwhile, in the [0/30/90] laminate, if the plateau value remains higher than the microcracking toughness, then the stitch crack will continue to propagate to form a long developed crack. Further comparison is shown in Fig. 4, where the $[0/60/90]_s$ laminate is under 1% strain and the $[0/30/90]_s$ laminate is under 1.2% strain. It can be seen that the SERR in the $[0/30/90]_s$ laminate requires more strain to reach the same peak value as in the $[0/60/90]_s$ laminate, i.e., the onset strain of the stitch crack in the $[0/30/90]_s$ is greater than that in the $[0/60/90]_s$. And once it reaches same value, the SERR in the $[0/30/90]_s$ remains higher than in the $[0/60/90]_s$. A typical value of G_{mc} (240 J/m^2) for epoxy

material has been taken [21]. It can be seen that under displacement controlled loading, the SERR in the $[0/60/90]_s$ drops below G_{mc} at a_c, which gives the stitch crack length at the current strain state. Meanwhile, the SERR in the $[0/30/90]_s$ is always greater than G_{mc} as a increases, which means that the stitch crack will continue to propagate to become a developed crack at this strain state. This confirms the results of experiments and analysis performed by Yokozeki et al. [17-19]

Another phenomenon observed by Yokozeki et al. [17-19] is that the thickness of the θ^o-ply affects the formation of the stitch crack. The thicker the θ^o-ply, the easier it is to form a developed crack instead of a stitch crack. Figures 5 and 6 show the effects of the thickness of the θ^o-ply on the SERR of stitch cracks. In Fig. 5, the $[0/60_n/90]_s$ laminate is investigated, the line with diamond symbols represents the SERR variation with respect to the stitch crack length in the $[0/60/90]_s$ under $\varepsilon_x = 1\%$ and the line with square symbols represents the SERR variation in the $[0/60_2/90]_s$ under $\varepsilon_x = 0.8\%$. It can be seen that even under lower strain level, the SERR in the $[0/60_2/90]_s$ is much greater than that in the $[0/60/90]_s$ and the stitch crack length a_c is much greater in the $[0/60_2/90]_s$. For the $[0/30_n/90]_s$ laminates, the same tendency can be found. As shown in Fig. 6, the SERR in the $[0/30_2/90]_s$ under 0.8% strain is greater than that in the $[0/30/90]_s$ under 1.2% strain. The developed cracks are developed in both laminates.

In the following, the effects of spacing l_x and l_y will be investigated. First the variation of SERR with respect to l_x in $[0/60/90]_s$ is computed by fixing $a = 0.6$ mm and $l_y = 1.0$ mm as shown in Fig. 7. The J-integral method is used to compute the SERR. It can be seen that the SERR almost remains at the same level, which means that the spacing l_x does not affect the SERR of stitch crack so much.

Next, the SERR for generating new stitch cracks is computed, i.e., the effects of l_y on the SERR is studied for fixed a (0.6 mm) and l_x (2.5 mm). Since we assume that the stitch cracks are evenly distributed, the new stitch crack has to appear at the middle position between two existing cracks. Hence, one unit cell becomes two, and the spacing l_y reduces to half, as shown in Fig. 8A. In this case, the old cracks will not propagate and the released strain energy is due to the newly formed crack, hence the J-integral method is not applicable any more. So the SERR is computed using the definition of the strain energy release rate. Figure 8B shows the variation of the computed SERR, which tells us that the SERR remains constant for large l_y and then drops down significantly as l_y goes to zero. This means that once stitch cracks appear, they will accumulate very fast until saturation occurs.

PREDICTION OF GAS PERMEABILITY

In our previous work [11], the gas permeability of cross-ply laminates was derived from Darcy's Law for porous materials as

$$k = \frac{Ch}{h_1/\left(\lambda_1\lambda_2 A_{(1,2)}\right) + \sum_{i=2}^{N-1} 2h_i/\left(\lambda_{i-1}\lambda_i A_{(i-1,i)} + \lambda_i\lambda_{i+1} A_{(i,i+1)}\right) + h_N/\left(\lambda_{N-1}\lambda_N A_{(N-1,N)}\right)} \quad (2)$$

where λ_i and h_i are the crack density and the ply thickness of the i^{th} ply, respectively; h is the thickness of the laminate; $A_{(i,\,i+1)}$ is the intersection area between the i^{th} ply and $(i+1)^{\text{th}}$ ply (as shown in Fig. 9); and C is a material constant to be determined by experiments.

Based on the assumption that the gas permeability is mainly determined by the total intersection area between layers, this permeation model can be easily extended to multidirectional laminates. The difference between multidirectional laminates and cross-ply laminates is the way to compute number of intersections and the intersection

area. As shown in Fig. 10, instead of a rectangle, the intersection area formed by the cracking openings of stitch cracks and transverse cracks in the 90^o-ply is now a parallelogram. Hence the intersection area A is given by $d_1 \times d_2/\cos\theta$.

Under biaxial loading, cracks are generated in every layer of the multidirectional laminate. Compared to cross-ply laminate, there are more scenarios in multidirectional laminates because of the stitch cracks in the angle ply. In this work, we consider a special scenario in the $[0/\theta/90]_s$ laminate as shown in Fig. 11. In this scenario, we assume that the cracks in the 0^o, 90^o and θ^o-ply are all evenly distributed and characterized by crack densities. Stitch cracks formed in the angle ply have same crack length and one stitch crack is assumed to interact only once with the transverse cracks in the 0^o-ply and/or the 90^o-ply. We assume that there is always one stitch crack at the cross-point between transverse cracks in the 0^o-ply and the 90^o-ply (Figure 11). In this case, only the stitch cracks at the cross-points will connect the transverse cracks in the 0^o-ply and the 90^o-ply to form the contiguous gas leak pathway. In another word, the number of intersections is only related to the crack densities of the 0^o- and 90^o-ply.

The crack densities in the 0^o-ply and the 90^o-ply can be predicted using the method provided in Ref. [23]. The only difference is that the angle ply with stitch cracks should be included into the unit cell. Based on the fact that the transverse crack densities does not have much influence on the intersection area [11], in this work for simplicity and for comparison with the results in cross-ply laminate, the transverse crack densities in the 0^o-ply and the 90^o-ply are taken as the same crack densities predicted for the cross-ply $[0/90_4/0]$ laminate [23]. The crack densities under stress

ratio $A = N_x/N_y = 0.5$ was predicted and presented in Fig. 12 using the method developed by Bapanapalli, et al. [24]

To compute the intersection area, a unit cell shown in Fig.13 is taken, whose dimensions are determined by the crack densities in the 0^o- and 90^o-ply. In this figure all the shaded areas are crack surfaces. Delaminations with a length of 0.14 mm from both the 0^o- and 90^o-ply are introduced in this model (not shown in Fig. 13). The crack densities in the 0^o- and 90^o-ply are taken as 2 cm^{-1}. From the aforementioned discussion, only the stitch crack at the cross-point of the transverse cracks in the 0^o-ply and the 90^o-ply will be part of the contiguous leak pathway. So it is reasonable to only model the stitch cracks at the cross-points. The results for the $[0/60/90]_s$ laminate shown in Table II support this argument. In this table, the intersection areas between the 90^o-ply and the 60^o-ply are computed for unit cells with different numbers of stitch cracks along the transverse cracks in the 90^o-ply. The unit cells are loaded under same condition ($\varepsilon_x = 1\%$, $\varepsilon_y = 0$). As we can see, as the numbers of the stitch cracks increase from 1 through 4, the intersection areas do not change so much. The difference is less than 1%.

In Fig. 14, the intersection areas in $[0/60/90]_s$ are computed as a function of the stitch crack length under the same loading condition (Case I: $\varepsilon_x = 1\%$, $\varepsilon_y = 0$; Case II: $\varepsilon_x = 0$, $\varepsilon_y = 1\%$). The stitch crack length ($2a$) increases from 1.2 mm to 2.8 mm. Unlike the delamination length, the length of stitch crack does not have much influence on the intersection areas. The intersection areas increase by a small amount as the stitch crack length increases. When the stitch crack length increases by 133%, the increment of intersection area is less than 5%. Under both loading cases, the

intersection areas between the 90^o-ply and the 60^o-ply are larger than the areas between the 60^o-ply and the 0^o-ply.

Following the procedure to predict the progressive permeability in cross-ply laminates, the normalized permeabilities in the $[0/60/90]_s$ laminate and the $[0/30/90]_s$ are predicted as a function of applied stress in Fig. 15. In Fig. 15, the line with cross symbols represents the permeability in the $[0/60/90]_s$ laminate and the line with triangle symbols represents the permeability in the $[0/30/90]_s$ laminate. For comparison, the permeability predicted in $[0/90_4/0]$ is also plotted in Fig. 15. It can be seen that the permeabilities in the $[0/60/90]_s$ and in the $[0/30/90]_s$ are much less than that in the $[0/90_4/0]$ even though they have the same number of layers and the same crack densities. This is because that the intersection areas between stitch cracks and transverse cracks are much smaller than the intersection areas between transverse cracks. The permeability in the $[0/30/90]_s$ is slightly higher than that in the $[0/60/90]_s$.

The permeability is also plotted as a function of strain as shown in Fig. 16. In this figure, the permeabilities in the $[0/60/90]_s$ and the $[0/90_4/0]$ laminates are about the same for a given strain (< 0.55%), and the permeability in $[0/30/90]_s$ is higher than them. But, the permeability in $[0/90_4/0]$ still has greater increasing trend under higher strains. There are two reasons that can explain this. One is that the lay-up in $[0/\theta/90]_s$ is dispersed and that in $[0/90_4/0]$ is grouped. From our previous work [11], for a given laminate thickness, the dispersed lay-up has lower permeability than the grouped lay-up. Another reason is that the intersection areas in $[0/\theta/90]_s$ is smaller than the intersection areas in $[0/90_4/0]$.

SUMMARY AND CONCLUSIONS

In the present work, the damage evolution and the permeability in multidirectional laminate is investigated. From this study, it has been found that the variations of the strain energy release rate with respect to the stitch crack length largely depend on the fiber direction and the thickness of the angle-ply, which explains the experimental observations in the literature. The thermal effect can significantly increase the total strain energy release rate in stitch cracks.

The permeation model developed in the previous work is extended to predict the permeability in multidirectional laminates. The intersection area computed in the unit cell of the multidirectional laminate is not affected by the number of stitch cracks in the unit cell and the stitch crack length. The permeability predicted in multidirectional laminates is much less than that in cross-ply laminate with the same transverse crack densities and the same number of layers.

In this study, however, an ideal unit cell is taken to simplify the prediction procedure. Hence, in the future, some statistical tools may be used to obtain more realistic unit cell dimensions. Finally, some experimental work needs to be performed to verify the predictions and quantify the material constant involved in the expression of permeability.

ACKNOWLEDGEMENT

This work was supported by NASA Glenn Research Center (NAG3-2750) and NASA Kennedy Space Center under the Hydrogen Research and Education Program. The authors gratefully thank their technical and financial support.

REFERENCES

1. Stokes E. Hydrogen Permeability of Polymer Based Composite Tank Material under Tetra-Axial Strain. In: Proceedings of 5th conference on aerospace materials, processes and environment technology (AMPET), Huntsville, Al, US, Sept., 2002.

2. Nettles AT. Permeability Testing of Impacted Composite Laminates for Use on Reusable Launch Vehicles. NASA/TM-2001-210799.
3. McManus HL, Faust A, Uebelhart S. Gas Permeability of Thermally Cycled Graphite-epoxy Composites. In: Proceedings of 16th ASC Technical Conference. Blacksburg, VA, US, Sept., 2001. ASC-2001-092.
4. Grenoble RW, Gates T. Hydrogen Permeability of Polymer Matrix Composites at Cryogenic Temperatures. In: Proceedings of 46th AIAA/ASME/ASCE/AHS/ASC Structures, Structural Dynamics & Materials Conference. Austin, TX, April, 2005. AIAA-2005-2086.
5. Bechel VT, Camping JD, Kim RY. Cryogenic/elevated Temperature Cycling Induced Leakage Paths in PMCs. Composites: Part B 2005; 36(2):171-182.
6. Choi S. Micromechanics, Fracture Mechanics and Gas Permeability of Composite Laminates for Cryogenic Storage Systems. PhD Dissertation, University of Florida, 2005.
7. Aoki T, Kumazawa H, Susuki I. Propellant Leakage through Laminated Structures. In: Proceedings of 17th ASC Technical Conference. West Lafayette, IN, US, Oct., 2002.
8. Kumazawa H, Aoki T, Susuki I. Analysis and Experiment of Gas Leakage through Composite Laminates for Propellant Tanks. AIAA Journal 2003. 41(10):2037-2044.
9. Kumazawa H, Hayashi H, Susuki I, Utsunomiya T. Damage and Permeability Evolution in CFRP Cross-Ply Laminates. Composite Structure 2006. 76(1-2):73-81.
10. Roy S, Benjamin M. Modeling of Permeation and Damage in Graphite-epoxy Laminates for Cryogenic Fuel Storage. Composites Science and Technology 2004. 64(13-14):2051-2065.
11. Xu JL, Sankar BV. Parametric Investigation of Gas Permeability in Cross-Ply Laminates Using Finite Elements. AIAA Journal 2007. 45(4):934-941.
12. Noh J, Whitcomb J, Peddiraju P, Lagoudas D. Prediction of Leakage Rate through Damage Network in Cryogenic Composite Laminates. In: Proceedings of 45th AIAA/ASME/ASCE/AHS/ASC Structures, Structural Dynamics & Materials Conference. Palm Springs, CA, US, April, 2004. AIAA-2004-1861.
13. Peddiraju P, Lagousdas D, Noh J, Whitcomb J. Numerical Modeling of Cryogen Leakage through Composite Laminates. In: Proceedings of 45th AIAA/ASME/ASCE/AHS/ASC Structures, Structural Dynamics & Materials Conference. Palm Springs, CA, US, April 2004. AIAA-2004-1862.
14. Peddiraju P, Grenoble R, Fried K, Gates T, Lagoudas D. Analytical Predictions and Experimental Measurements of Hydrogen Permeability in a Microcrack Damaged Composite. In: Proceedings of 46th AIAA/ASME/ASCE/AHS/ASC Structures, Structural Dynamics & Materials Conference. Austin, TX, US April 2005. AIAA-2005-2087.
15. Roy S, Nair A. Modeling of Permeability in Composite Laminates with Delaminations and Stitch Cracks. In: Proceedings of 47th AIAA/ASME/ASCE/AHS/ASC Structures, Structural Dynamics & Materials Conference. Newport, RI, US, May 2006. AIAA-2006-2094.
16. Lavoie JA, and Adolfsson E. Stitch Cracks in Constraint Plies Adjacent to a Cracked Ply. Journal of Composite Materials 2001. 35(23):2077-2097.

17. Yokozeki T, Aoki T, Ogasawara T, Ishikawa T. Effects of layup angle and ply thickness on matrix crack interaction in contiguous plies of composite laminates. Composites: Part A 2005. 36(9):1229-1235.
18. Yokozeki T, Ishikawa T. Through-Thickness Connection of Matrix Cracks in Laminate Composites for Propellant Tank. Journal of Spacecraft and Rockets 2005. 42(4):647-653.
19. Yokozeki T, Aoki T, Ishikawa T. Consecutive Matrix Cracking in Contiguous Plies of Composite Laminates. International Journal of Solids and Structures 2005. 42(9-10):2785-2802.
20. Jamison RD, Schulte K, Reifsnider KL, Stinchcomb WW. Characterization and Analysis of Damage Mechanism in Tension-Tension Fatigue of Graphite/Epoxy Laminates. In: Wilkins DJ, editor. Effects of Defects in Composites Materials. West Conshohocken: ASTM International, 1984. p. 21-55.
21. Nairn JA. Matrix Microcracking in Composites. In: Talreja R, Manson JA, Editors. Polymer Matrix Composites. Chapter 13, p. 403-432. Volume 2 of Kelly A, Zweben C, Editors. Comprehensive Composite Materials. Elsevier Science, 2000.
22. Xu JL. Prediction of Gas Permeability in Composite Laminates using Finite Elements. PhD Dissertation. University of Florida. 2007.
23. Xu JL, Sankar BV, Bapanapalli SK. Finite Element Based Method to Predict Gas Permeability in Cross-ply Laminates. Journal of Composite Materials. (Submitted)
24. Bapanapalli SK, Sankar BV, Primas RJ. Microcracking in Cross-ply Laminates due to Biaxial Mechanical and Thermal Loading. AIAA Journal 2006. 44(12):2949-2957.

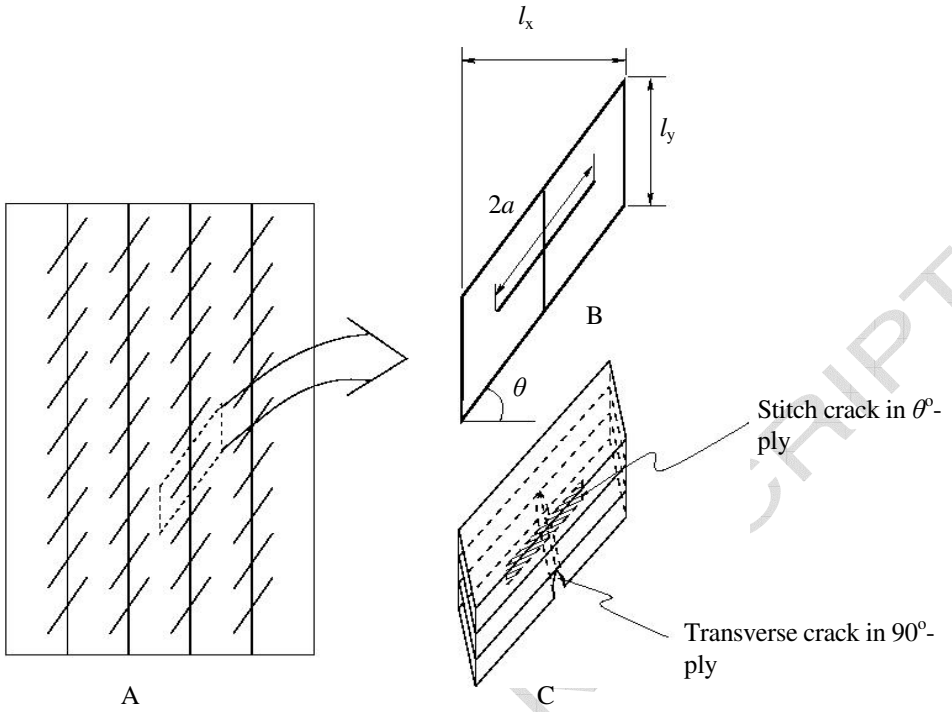

Figure 1. Unit cell taken from laminate $[0/\theta/90]_s$. A) Top view of laminate. B) Top view of the unit cell. C) Three-dimensional view of the half of the unit cell.

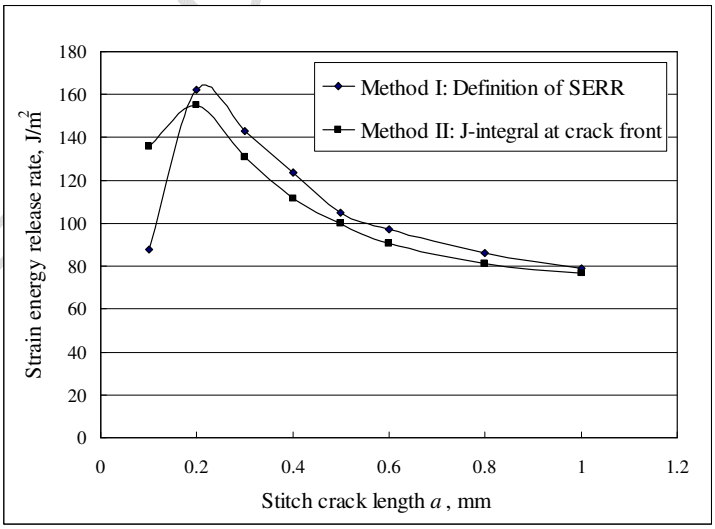

Figure 2. Comparison of strain energy release rate computed from two different methods.

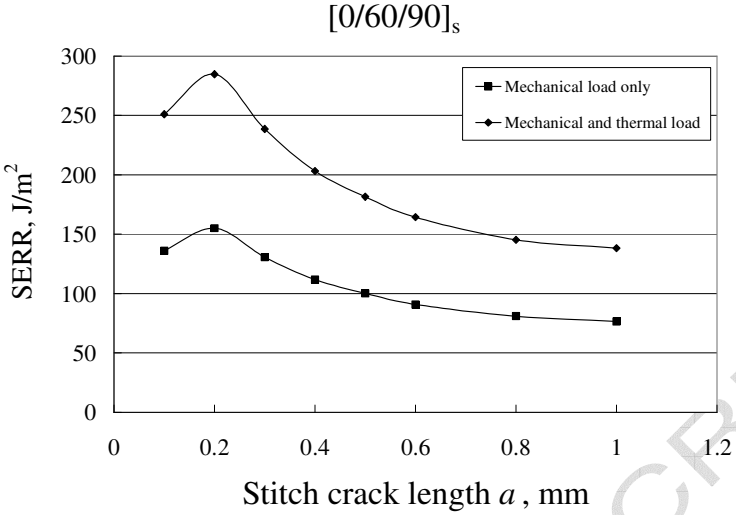

A

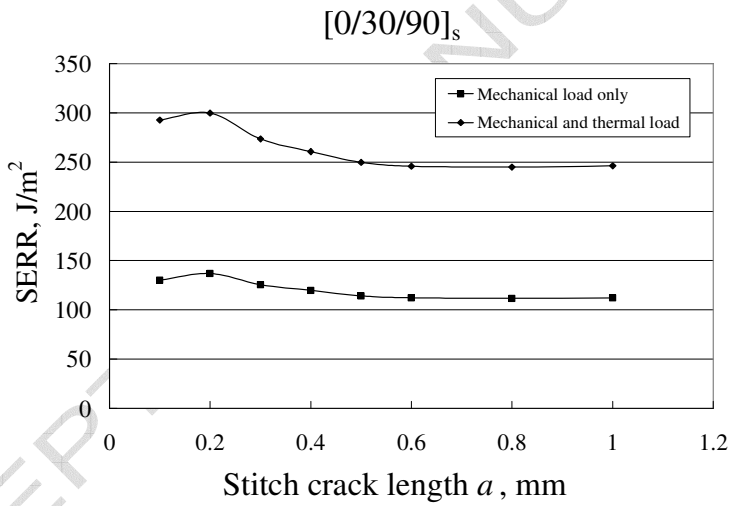

B

Figure 3: Thermal stress effect due to temperature difference between curing temperature and service temperature. A) $[0/60/90]_s$. B) $[0/30/90]_s$.

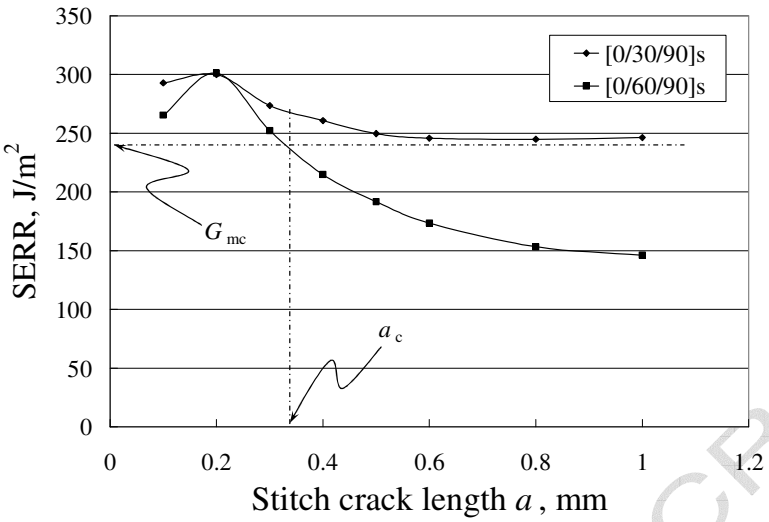

Figure 4. Effect of angle θ on the mechanism of formation of stitch crack.

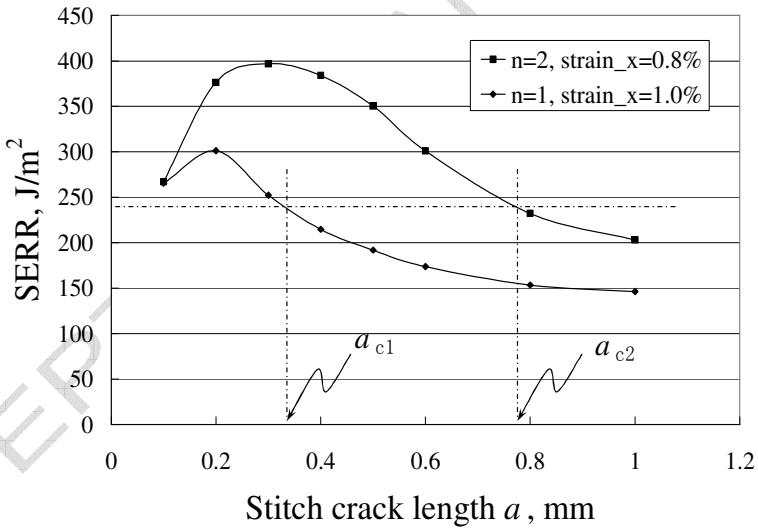

Figure 5. Effects of the thickness of angle plies in $[0/60_n/90]_s$.

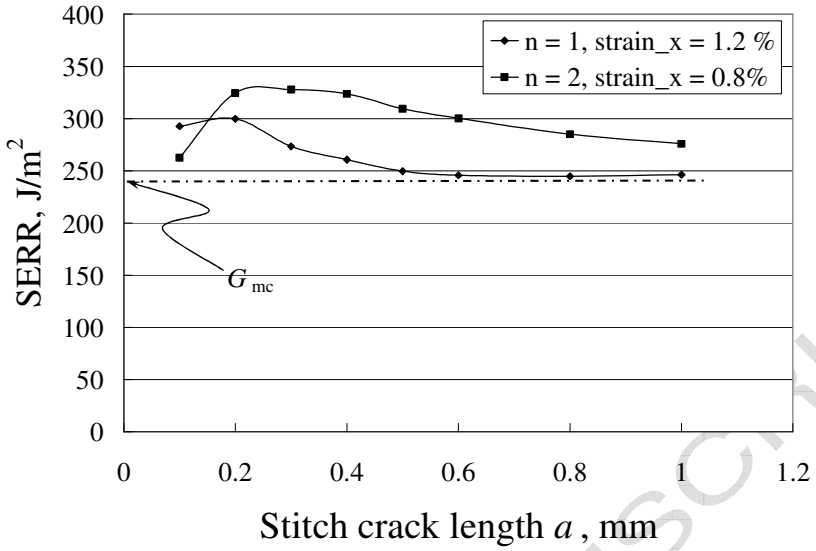

Figure 6. Effects of the thickness of angle plies in lay up $[0/30_n/90]_s$.

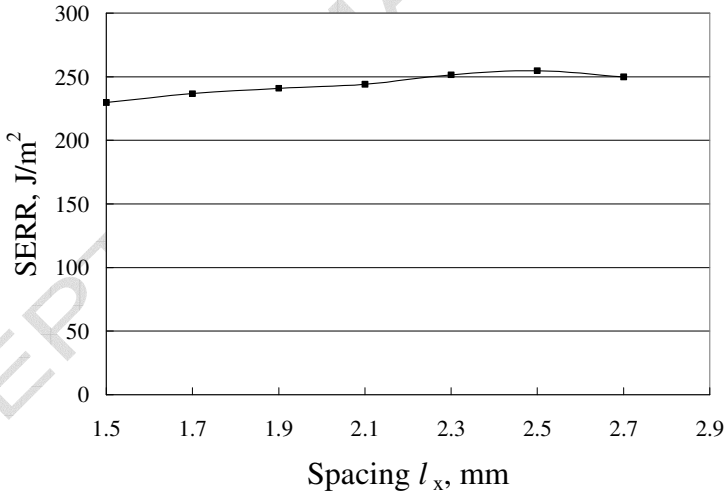

Figure 7. Effect of spacing l_x on the strain energy release rate of stitch crack.

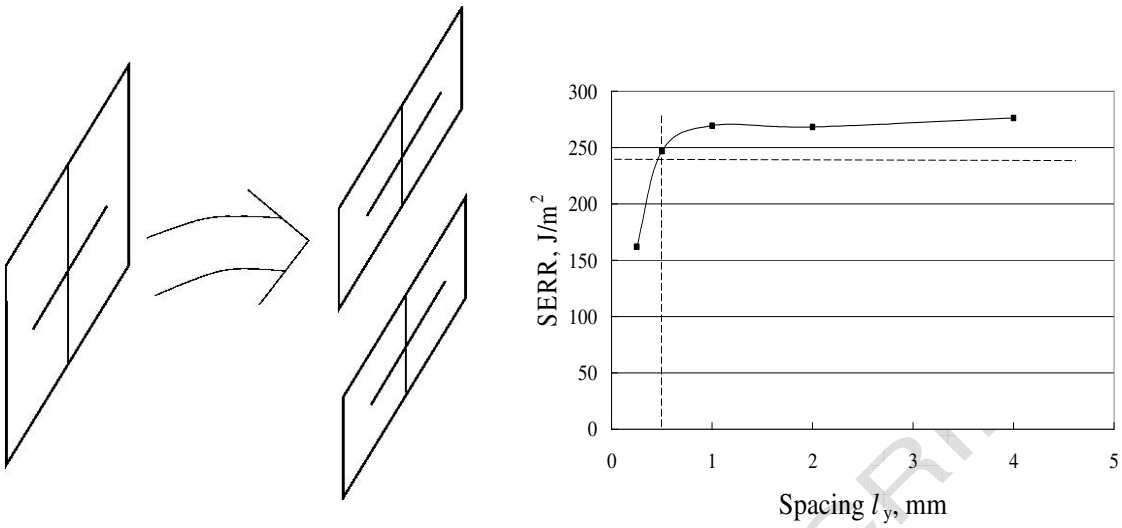

A B

Figure 8: Strain energy release rate related to the generation of new stitch crack. A) Formation of new cracks. B) Strain energy release rate variation.

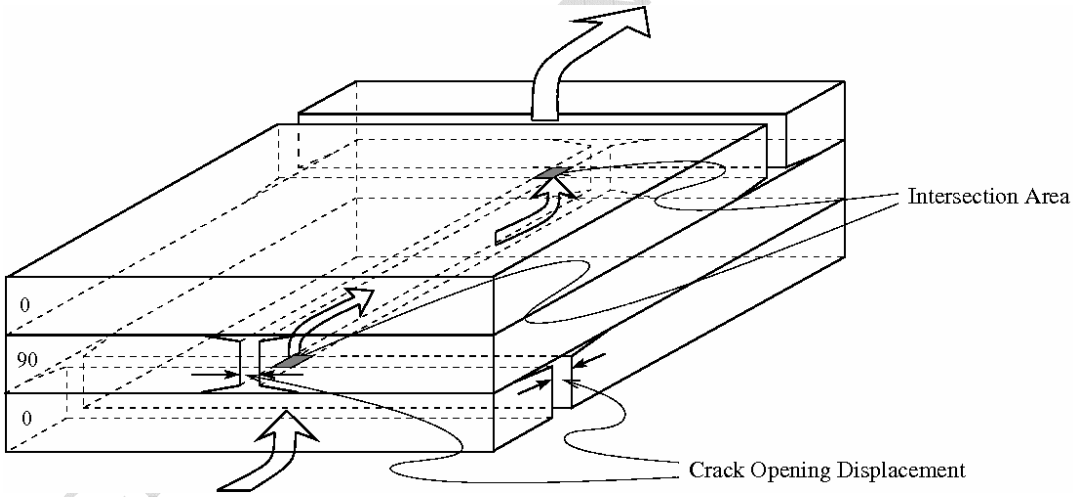

Figure 9: Gas permeation pathway provided by microcracks and delaminations in cross-ply laminates.

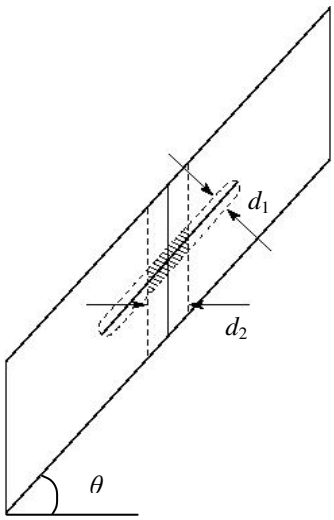

Figure 10: Intersection area formed by crack openings of stitch crack and transverse crack.

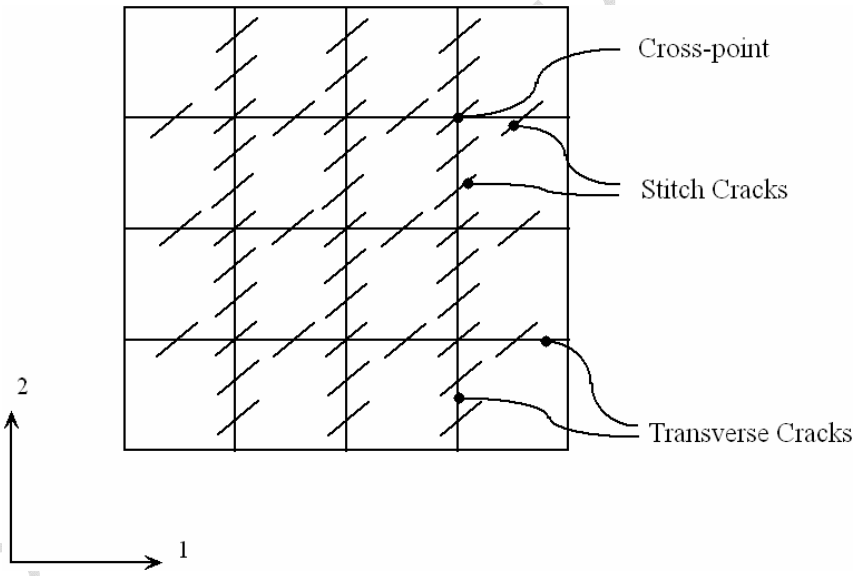

Figure 11: Special cracking scenarios in multidirectional laminates.

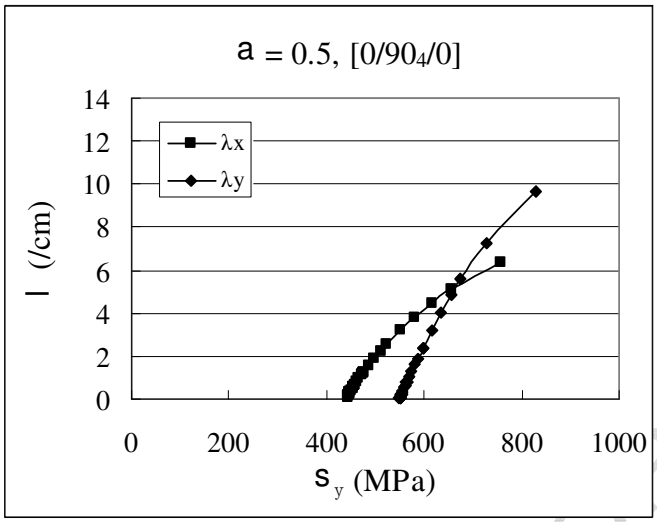

Figure 12: Crack densities predicted for laminate $[0/90_4/0]$. $N_x/N_y = 0.5$

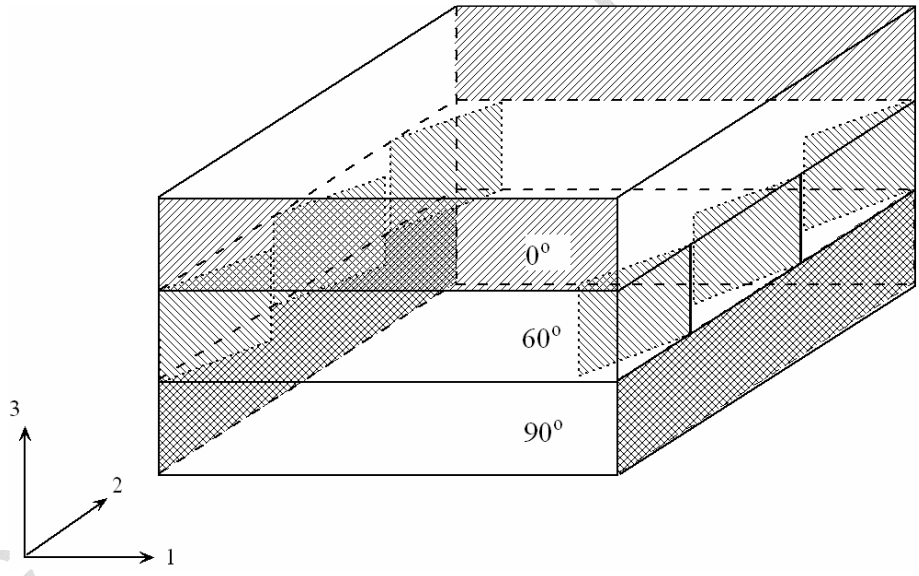

Figure 13: Unit cell for laminate with stitch cracks.

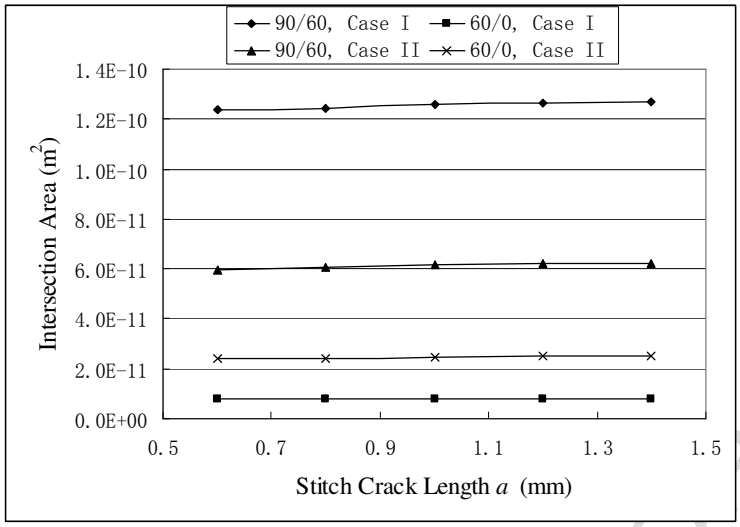

Figure 14: Effect of the stitch crack length on the intersection areas in $[0/60/90]_s$ laminate.

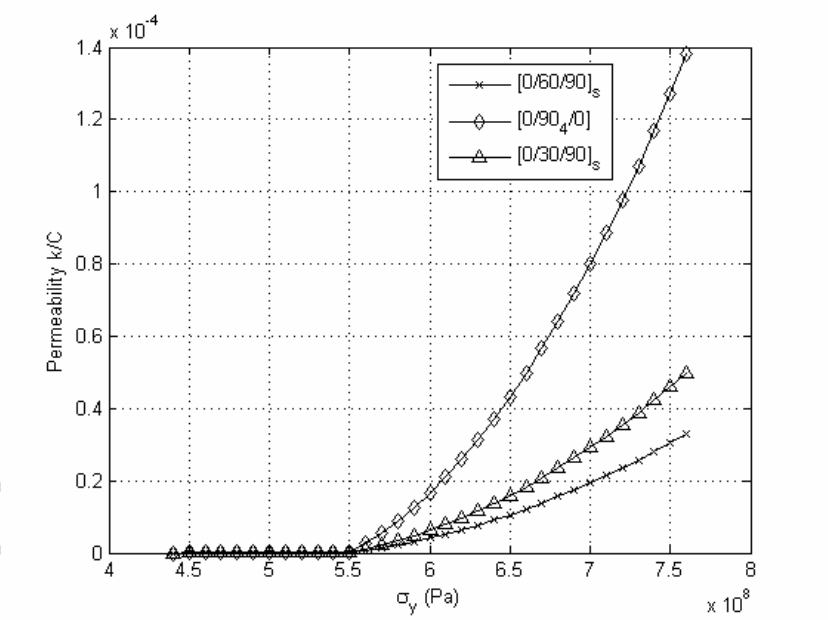

Figure 15: Permeability in laminate $[0/\theta/90]_s$ with stitch cracks and in [0/904/0] cross-ply laminate as a function of applied stress.

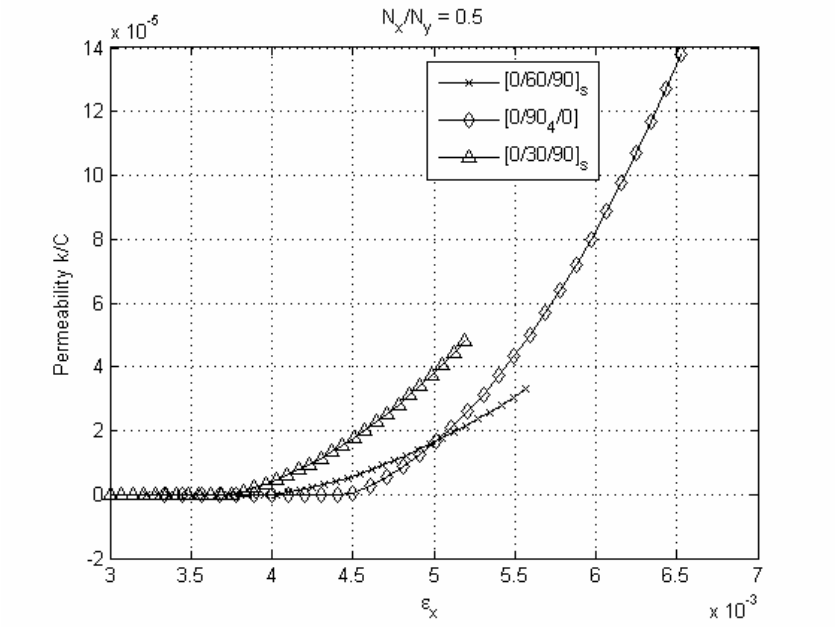

Figure 16: Permeability in [0/θ/90]$_s$ laminate with stitch cracks and in [0/90$_4$/0] cross-ply laminate as a function of applied strain.

Table I. Orthotropic material properties of the layers in the composite laminate.

E_1	169 GPa
E_2, E_3	8.62 GPa
G_{12}, G_{13}	5.0 GPa
G_{23}	1.22 GPa
ν_{12}, ν_{13}	0.355
ν_{23}	0.410
α_1	$-0.00338e^{-6}$ /°C
α_2, α_3	$29.00e^{-6}$/°C

Table II. Intersection areas in $[0/60/90]_s$ laminate for unit cells with different numbers of stitch cracks.

Number of stitch cracks	Intersection area (m^2)
1	6.1920E-11
2	6.1769E-11
4	6.1505E-11